Model Predictive Control of Large Scale Motions for Separated Flow Over an Airfoil

Akshit Jariwala* and Anton Burtsev†
The University of Texas at Austin, Austin, TX 78712

Saikishan Suryanarayanan ‡
The University of Akron, Akron, OH 44325

Efstathios Bakolas § and David Goldstein ¶
The University of Texas at Austin, Austin, TX 78712

Turbulent boundary layers (TBLs) are dominated by large-scale motions (LSMs) of streamwise momentum surplus and deficits. These LSMs carry a significant portion of turbulent kinetic energy and have the potential to alter flow behavior and mean statistics. This study extends the concept of selectively targeting LSMs to delay flow separation over an airfoil for improved aerodynamic performance. Large-eddy simulations were conducted for the flow over a NACA4412 airfoil at a moderate chord-based Reynolds number of 200,000 and an angle of attack of 10°. To achieve the desired TBL and generate the LSMs of interest, the boundary layer was tripped at 10% of the chord length using random volumetric forcing akin to sand-grain roughness. A model predictive control scheme was employed based on a reduced-order model of the flow, directing the LSMs towards the separated flow region optimally via body force-induced downwash. The effectiveness of this approach at reducing flow separation and its impact on lift and drag coefficient was examined. Results showed that targeting fast LSMs shows more performance improvement compared to targeting slow LSMs, random actuation, or constant actuation.

I. Nomenclature

$(\cdot)_x$	=	Quantity in streamwise direction
$(\cdot)_y$	=	Quantity in wall-normal direction
$(\cdot)_z$	=	Quantity in spanwise direction
L	=	Length of computational domain
N	=	Number of spectral elements
c	=	Chord length
δ	=	Boundary Layer thickness
θ	=	Momentum thickness
ν	=	Kinematic viscosity
α	=	Angle of Attack
Re_c	=	Reynolds number based on chord length
$\mathbf{V}$	=	Velocity vector [u, v, w]
$(\cdot)'$	=	Velocity fluctuations
V_∞	=	Free stream velocity magnitude
x	=	Streamwise coordinate
y	=	Wall-normal coordinate

*Graduate Student, Department of Aerospace Engineering and Engineering Mechanics, The University of Texas at Austin; Corresponding author, email: akshit@utexas.edu
†Postdoctoral Fellow, Department of Aerospace Engineering and Engineering Mechanics, The University of Texas at Austin
‡Assistant Professor, Department of Mechanical Engineering, The University of Akron
§Associate Professor, Department of Aerospace Engineering and Engineering Mechanics, The University of Texas at Austin
¶Professor, Department of Aerospace Engineering and Engineering Mechanics, The University of Texas at Austin

z	=	Spanwise coordinate
$\boldsymbol{e}_\phi$	=	Direction of the jet force field
ϕ	=	Pitch angle of the jet force field
$\mathbf{F}$	=	Body force field
$\mathbf{G}$	=	Jet power input
N_{meas}	=	LSM measurement frequency, in number of ROM timesteps
N_{mpc}	=	MPC horizon in number of ROM time steps
n_p	=	Number of control inputs
n_q	=	Number of points in measurement and control grid
n_r	=	Number of reduced-order model states
$\mathbf{u}(t)$	=	Control input at time step t
$\mathbf{u}^*_{t_1:t_2}$	=	Optimal control policy from time step t_1 to time step t_2
$\mathbf{z}(t)$	=	Reduced order state
$\mathrm{y}(t)$	=	v' at the control grid at time step t
m	=	Number of snapshots

II. Introduction

Large-scale motions (LSMs) are characterized by streamwise velocity fluctuations, creating regions of both momentum surplus and deficit within turbulent boundary layers (TBLs). These LSMs display significant temporal and spatial coherence, typically on the scale of the boundary layer thickness [1]. Spectral analysis of LSMs reveals their significant contribution to turbulent kinetic energy (TKE), Reynolds shear stress, and momentum transport within the boundary layer [2–6]. Given their statistical significance, LSMs can substantially influence boundary layer dynamics and alter flow behavior and patterns.

TBLs subjected to adverse pressure gradients (APGs), which are common in real-world engineering applications such as airfoils, rotor-craft, and turbo-machines, exhibit notable contributions from LSMs [7–11]. LSMs carrying surplus momentum have the potential to counteract the effects of APG and reduce the size of the separated flow region. Numerous flow control concepts exist that do not account for the presence of LSMs in APG environments. These include active control methods such as uniform suction and blowing [12, 13] and plasma actuators [14], as well as passive control methods like vortex generators and surface roughness.

We suggest that LSMs are ideal targets for novel flow control strategies aimed at separation delay by manipulating naturally occurring LSMs in a turbulent boundary layer. Previous studies have focused on targeting near-wall structures and LSMs in the log-region for drag reduction [15–19]. These efforts have yielded mixed results, primarily influencing drag but not significantly addressing separation. Recently, however, targeted manipulation of high-momentum LSMs has shown promise in re-energizing the boundary layer by increasing wall-shear stress and enhancing mixing [20, 21]. This was also tested in an experimental setting where a synthetic train of hairpin vortices, a model for a simple LSM, was moved towards the wall showing increased near-wall TKE and vorticity [22]. This approach leverages the inherent dynamics of LSMs to improve flow stability and reduce the extent of separated flow regions, offering a potentially more effective means of flow control in various aerodynamic applications.

This study extends the model predictive control (MPC) of high-momentum LSMs, previously applied to separated turbulent boundary layers (TBLs) over a flat plate, as demonstrated by Tsolovikos et al. [23] for flow over an airfoil. The proposed active control strategy consists of two main steps: (1) detecting the LSMs of interest upstream, and (2) deciding whether and when to actuate on these incoming LSMs. The decision to actuate is governed by an MPC policy, which involves: (1) predicting the downstream path of the LSM as it approaches the actuator, and (2) solving an optimal output tracking control problem. This problem utilizes a binary on/off input to the actuator, aiming to maximize the downwash experienced by the target LSM while minimizing the actuation cost. Further details on the optimal control problem can be found in Tsolovikos et al. [23].

The present study conducts a numerical investigation of the flow over a NACA4412 airfoil at a moderate chord-based Reynolds number of $Re_c = 200,000$ at an angle of attack of 10°. To establish the desired TBL and generate the relevant LSMs, the boundary layer was tripped at 10% of the chord length using random volumetric forcing [24]. Discrete actuation was implemented using a near-wall jet modeled as a body force field, with a Gamma distribution in the streamwise direction and a Gaussian distribution in the wall-normal and spanwise directions. This approach, illustrated in Figure 1, is inspired by the effects of dielectric barrier plasma actuators [25] and jet-assisted surface-mounted actuators [26], which help entrain flow toward the wall. For simplicity, LSMs are detected upstream of the actuator by

applying a box filter to the three-dimensional streamwise velocity fluctuations.

The paper is structured as follows: Section III details the computational setup for the numerical simulations, including the tripping forces and the jet body force model. Section IV describes the reduced-order model (ROM) of jet-induced downwash, along with the MPC and optimal control methods. Section V presents preliminary results, highlighting the effects on lift and drag coefficients across the different cases under consideration.

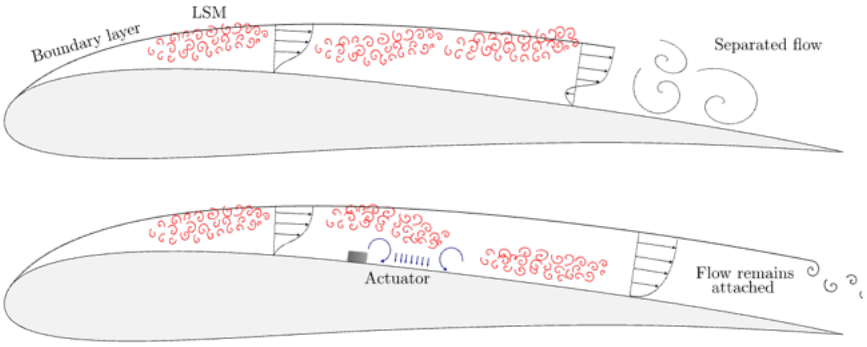

Fig. 1 Illustration of targeted manipulation of LSMs over an airfoil. Top: Flow without control, leading to separation. Bottom: Flow remains attached due to controlled LSMs.

III. Numerical Setup

A. Large-Eddy Simulation

This study employs a filtering-based large-eddy simulation (LES) for flow over a NACA4412 airfoil using high-order spectral element solver NEK5000 [27, 28]. The incompressible Navier-Stokes and continuity equations

$$\frac{\partial \mathbf{V}}{\partial t} + \mathbf{V} \cdot \nabla \mathbf{V} = -\nabla P + \frac{1}{Re_c} \Delta \mathbf{V} + \mathbf{F}_{\text{Trip}} + \mathbf{F}_{\text{Jet}} \tag{1}$$

$$\nabla \cdot \mathbf{V} = 0 \tag{2}$$

are non-dimensionalized by the free-stream velocity, V_∞, and the chord length of the airfoil. The position $\mathbf{X} = [x,\ y,\ z]$ and velocity $\mathbf{V} = [u,\ v,\ w]$ vectors consist of their streamwise, wall-normal, and spanwise components, respectively.

The computational domain has dimensions of $L_x \times L_y \times L_z = 30c \times 20c \times 0.05c$, with a total of $N = 80,000$ spectral elements. Each of these spectral elements uses a $\mathbb{P}_N = 7$-th order Gauss-Lobatto-Legendre polynomial ($\mathbb{P}_N - \mathbb{P}_{N-2}$ formulation) to represent the velocity and pressure fields. A second-order backward difference explicit-implicit time integration scheme was used with timestep $dt = 1.0e^{-4}c/V_\infty$. Figure 2 illustrates the computational domain and the spectral element grid near the airfoil surface. The boundary conditions for the rest of the domain include a no-slip condition at the wall, periodic boundary conditions in the spanwise direction, and an outflow boundary condition $[-PI + \nu(\nabla \mathbf{V})] \cdot \mathbf{n} = 0$ at the top, bottom, and outlet, where $\mathbf{n}$ denotes the normal outward vector. The inlet boundary, which is the left-hand semi-circular portion of the domain, has a free stream velocity vector $\mathbf{V}_\infty = [V_\infty \cos\alpha, V_\infty \sin\alpha, 0]$ where α is angle of attack for the airfoil and V_∞ is freestream velocity magnitude.

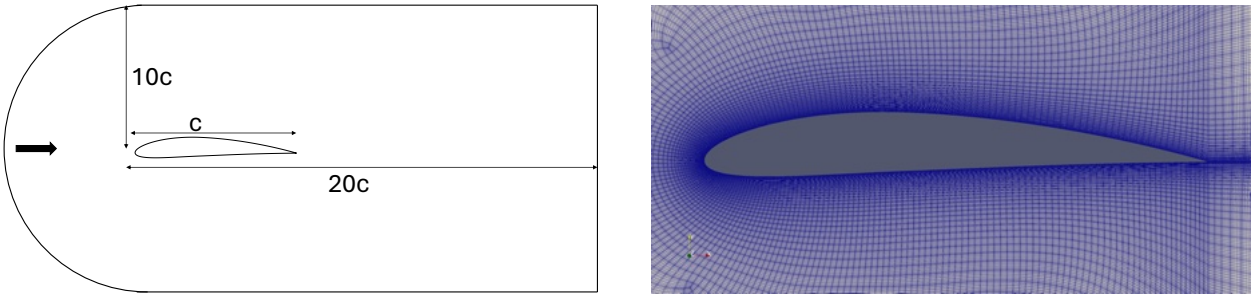

(a) Computational domain **(b) Grid close to the airfoil surface**

Fig. 2 Size of the computational domain and the grid representation

1. Boundary Layer Tripping

To achieve TBLs on the suction side of the airfoil surface, the boundary layer was tripped at 10% of the chord length using random volumetric forcing in the wall-normal direction [24]. The tripping method applies Gaussian-like distributed forces in the streamwise and wall-normal directions, modulated by a random harmonic function in the spanwise direction and over time [29]. These forces act primarily in the wall-normal direction to ensure the proper development of the turbulent boundary layer and have been shown to be effective at tripping the boundary layer at moderate Reynolds number [30, 31]. The tripping force fields are incorporated into the momentum equation (1) as $\mathbf{F}_{\text{Trip}}$. The tripping force field distribution near the leading edge of the airfoil is depicted in Figure 3a. Additionally, the downstream development of LSMs resulting from the boundary layer tripping is shown in Figure 3b, with positive streamwise velocity fluctuations visualized and colored by the streamwise velocity component.

2. Body Force Actuator

To entrain LSMs, a near-wall jet was modeled as a body force field. This jet force field follows a Gamma distribution in the streamwise direction and Gaussian distributions in both the wall-normal and spanwise directions. The jet is pitched downstream at an angle ϕ such that it acts tangent to the airfoil surface. The jet force field can be described as

$$\mathbf{F}_{\text{Jet}} = \boldsymbol{e}_{\phi}\tilde{g}(\mathbf{X})\tilde{f}(t) \tag{3}$$

In the above, $\boldsymbol{e}_{\phi} = [\cos\phi, \sin\phi, 0]$ is the direction of the force field with pitch angle $\phi = -45°$. The angle is empirically chosen to create an equal amount of localized near-wall downwash and flow acceleration. $\tilde{g}$ is the spatial force field distribution that is given by,

$$\tilde{g}(\mathbf{X}) = \begin{cases} g(\mathbf{X}) & \text{if } g(\mathbf{X}) > 0.01, \\ 0 & \text{otherwise,} \end{cases} \tag{4}$$

where,

$$g(\mathbf{x}) = \frac{x - x_{\text{Jet}}}{\sigma_x} \cdot \exp\left(1 - \frac{x - x_{\text{Jet}}}{\sigma_x}\right) \cdot \exp\left(-\frac{1}{2}\frac{(y - y_{\text{Jet}})^2}{\sigma_y^2}\right) \cdot \exp\left(-\frac{1}{2}\frac{(z - z_{\text{Jet}})^2}{\sigma_z^2}\right) \tag{5}$$

Here, $[x_{\text{Jet}}, y_{\text{Jet}}, z_{\text{Jet}}]$ denotes the centroid location of the jet field, with $\sigma_x = 0.02$, $\sigma_y = 0.01$, and $\sigma_z = 0.00625$ in chord units specifying the extents in the streamwise, wall-normal, and spanwise directions, respectively. These values are chosen such that the wall-normal extent of the jet approximately matches the local boundary layer thickness, ensuring effective targeting and influence on the LSMs in the outer layer. The streamwise extent is less critical, as the length of the downwash can be adjusted by controlling the duration for which the jet is active. The spanwise extent is selected such that the width of the downwash is proportional to the size and width of the LSMs, approximately 1–2%c [32]. Lastly, the scalar function $\tilde{f}(t)$ varies with time and governs the magnitude of the jet, where $\tilde{f}(t) = 0$ corresponds to the jet being turned off, and $\tilde{f}(t) = 1$ corresponds to the jet being turned on.

The jet is placed at 60% of the chord, with the rationale for this position being twofold. First, it is sufficiently far from the separated flow to minimize direct interaction between the induced flow acceleration and the separation region. Second, it is positioned downstream of the trip to allow proper development of LSMs on the suction side, while

remaining close enough for the LSMs to exert influence effectively. The jet force field distribution over the suction side of the airfoil at 60%c is shown in Figure 3a, in dark grey contour. Figure 4 illustrates the jet-induced downwash and upwash, represented as wall-normal velocity fluctuations at a specific contour level after being active for $\Delta t = 0.1c/V_\infty$. These velocity fluctuations are obtained by ensemble-averaging the turbulent flow snapshots, effectively isolating the jet's influence from the background turbulence, a total of 8 ensembles were used. As observed, the approximate length of the downwash region is about 10%c, corresponding to 10% of the chord-based time units. Thus, it can be concluded that the total length of the induced downwash region is approximately proportional to the total duration for which the jet remains active.

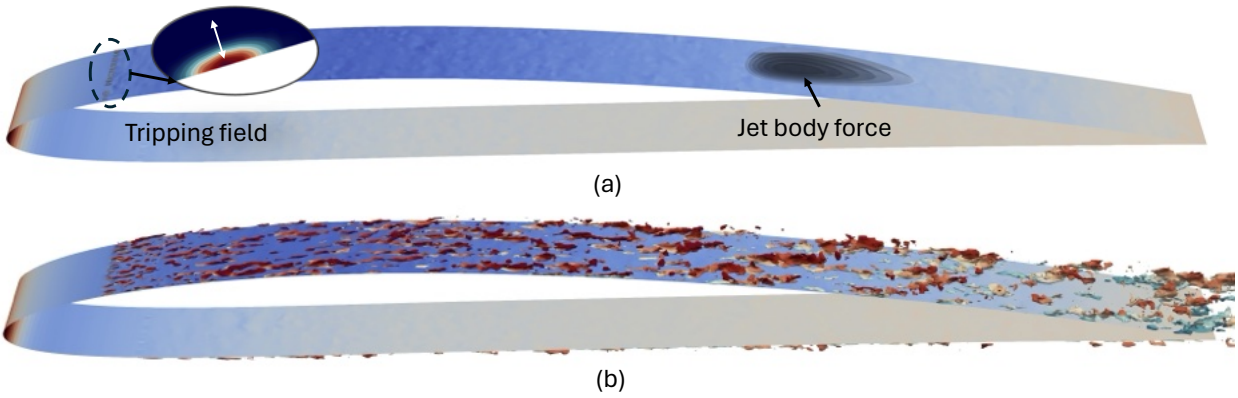

Fig. 3 (a) The tripping force field used to generate the TBL is shown in dark gray contours at 10% of the chord length, while the jet body-force field, which entrains the LSMs, is shown in dark gray contours at 60% of the chord length. (b) Contour plot of positive u' fluctuations highlighting LSMs with regions of momentum surplus in red.

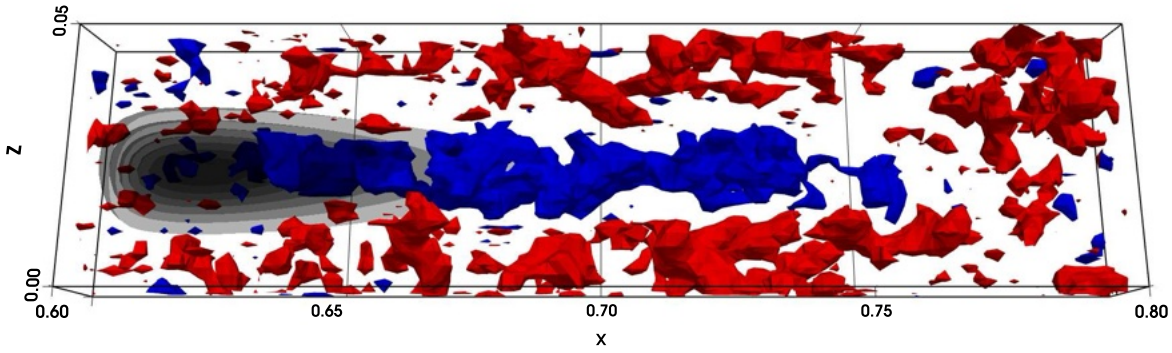

Fig. 4 Wall-normal velocity fluctuations induced by the jet: downawash $v' = -0.05$ in blue, upwash $v' = 0.04$ in red, and jet body force in dark grey isocontour

IV. Control Scheme

Since the objective of the proposed work is to direct LSMs toward the separated flow to enhance aerodynamic performance, a robust controller is required to: (1) identify the LSMs, (2) predict their downstream trajectory, and (3) induce a sufficiently strong downwash to alter their path. The details of LSM detection within the measurement grid upstream of the jet and their trajectory prediction using Taylor's hypothesis are outlined in the following subsection. The jet-induced wall-normal velocity fluctuations are modeled using a surrogate linear reduced-order model (ROM) that

captures the dynamics of jet actuation. Finally, the optimal output tracking control problem is formulated as a quadratic optimization problem to compute the optimal control sequence that signals the jet to turn on or off.

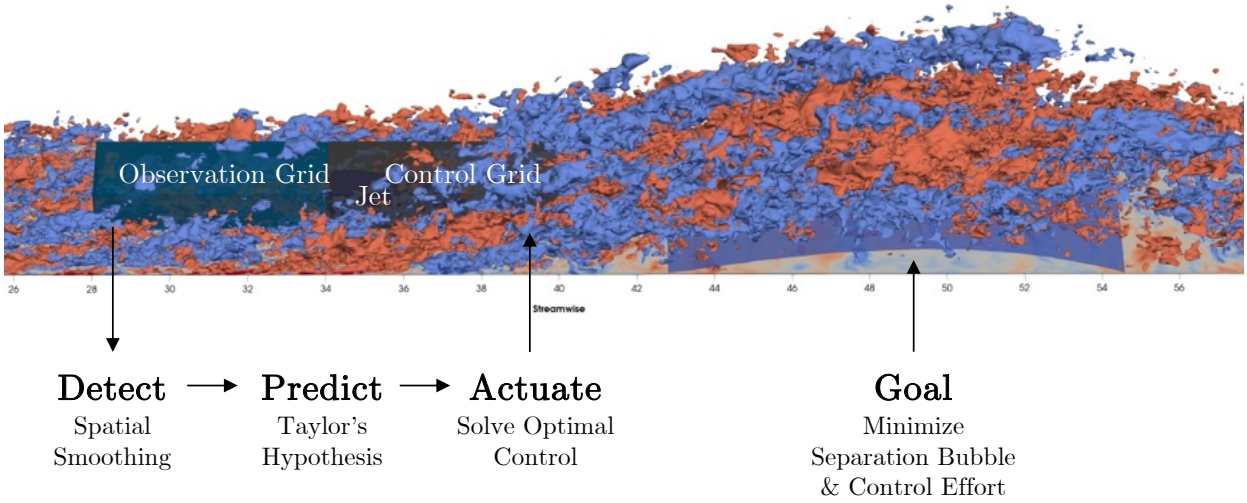

Fig. 5 Control scheme highlighting the observation grid for detecting LSMs, prediction steps for estimating the future location of LSMs, and the control grid indicating the region of body force application (adapted from Tsolovikos et al. [33]).

Figure 5 illustrates the overall control methodology. The observation grid identifies regions of interest, specifically targeting faster-moving LSMs. Once these LSMs are detected, the MPC model predicts their future trajectories. Based on these predictions, the optimal control scheme designs a control policy (sequence of control inputs) to steer the LSMs toward the separated flow with minimal control effort. The control grid encompasses the area where LSM locations are predicted and defines the region for applying the body force for jet actuation. This body force, regulated by the optimal control policy, enables effective manipulation of LSMs to achieve the flow control objectives.

A. Measurement and Prediction

The first step in the optimal control formulation is the identification of LSMs upstream of the jet. This is achieved by measuring raw streamwise velocity fluctuations, u', subsampled onto a measurement grid consisting of a collection of collocation points. The orthogonal observation grid consists of a total of $n_q = 101 \times 21 \times 21$ points in the streamwise, wall-normal, and spanwise directions, respectively, spanning $\Delta x = 0.1c$ from $x = 0.5c$ to $x = 0.6c$, $\Delta y = 0.01c$, and $\Delta z = L_z$. The y extent of the measurement grid captures the log-region and outer layer, where LSMs are known to be present. The grid is also rotated such that it is parallel to the local airfoil surface.

Once the velocity measurements are obtained, a simple box-filtering operation is performed to eliminate unwanted small-scale turbulent structures from the data. The box filter applies a $5 \times 5 \times 5$ uniform convolution kernel at each grid point in the measurement grid, acting as a low-pass filter to suppress background turbulence noise and smooth the data. This smoothing operation has been shown to be effective in enhancing the correlation between the filtered velocity fluctuations and their downstream counterparts when predicted using Taylor's hypothesis [23]. The filtering approach is illustrated in Figure 7, where it is clearly noticeable that small-scale structures are successfully eliminated, preserving only the larger structures that are easier to predict.

Once detected, an LSMs' position is predicted using Taylor's hypothesis of frozen turbulence, which assumes that velocity fluctuations are transported with the mean flow field. Over an airfoil, this is approximated by the time-averaged, unperturbed velocity field without actuation. According to Taylor's hypothesis, small-scale turbulent structures are convected downstream with the local mean velocity, as they can be treated as separate entities [34]. For relatively small time delays, this approximation has been shown to hold for the convection of u' fluctuations using mean velocities in the streamwise and wall-normal directions [35]. An illustration of the detection or measurement grid is presented in Figure 6, depicted as a translucent box upstream of the jet, which is shown in the dark gray contour.

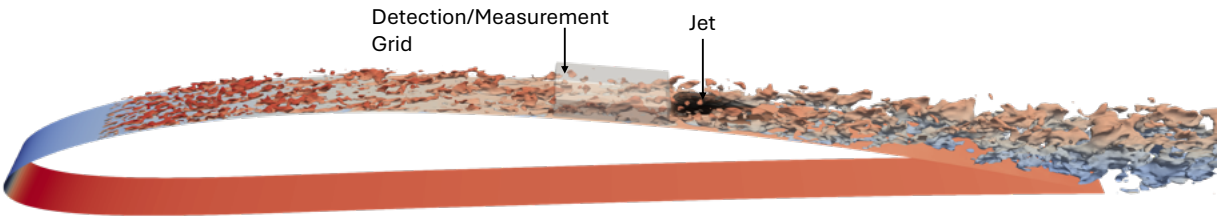

Fig. 6 Illustration of the detection or measurement grid (translucent box) positioned upstream of the jet (dark gray contour)

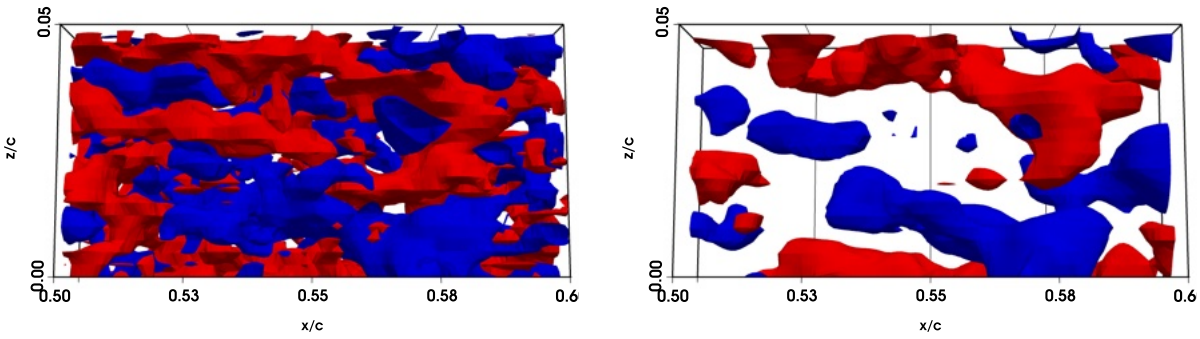

(a) Measured raw unfiltered u' in the detection region **(b) Filtered u' using a $5 \times 5 \times 5$ box convolution kernel filter**

Fig. 7 Streamwise velocity fluctuations, u', before (a) and after (b) filtering. Positive fluctuations are shown in red, and negative fluctuations are shown in blue, using the same threshold for both cases

B. Controller Reduced-Order Model

Once the LSMs' future positions are predicted using Taylor's hypothesis, the jet-induced downwash entrains them, directing them toward the separated region. The interaction between the predicted positions of the LSMs and the jet body force is modeled using a surrogate linear ROM. The dynamics are derived using the total least squares dynamic mode decomposition with control (tlsDMDc) method, which captures the linear relationship between the jet actuation strategy and its effects on the generated downwash, particularly fluctuations in the wall-normal velocity components. The ROM's time-invariant nature makes it highly effective for use in the later stages of the optimal control policy, offering a computationally efficient means to predict and influence LSM behavior for flow control. This integration ensures that the LSMs are guided to desired locations with minimal control effort, thereby facilitating more effective management and suppression of flow separation.

To train the model, a sequence of three distinct pulses was used for testing, with periods of 25, 50, and 100 ROM time steps, where each ROM time step corresponds to $10dt$. Since the jet remains active for durations on the order of the LSM size, the pulse sizes were chosen to ensure the jet is active long enough to induce a downwash comparable to the size of the LSMs in the TBL. For training, a total of 475 snapshots were recorded and ensemble-averaged over eight different LES simulations to isolate the jet-induced downwash from background noise (Figure 4).

The output of the tlsDMDc is a reduced-order state-space model that captures the dynamics of the underlying linear relationships within the noisy dataset, such as turbulent boundary layers (TBLs) with mean flow fields and velocity fluctuations. This ROM effectively simplifies the complex interactions within the flow. Further details regarding tslDMDc is outlined in the following section.

The output of the ROM can be subsequently used as an input to determine the optimal control policy that minimizes the cost function, i.e., the minimum actuation cost of the jet body force while optimally moving the LSMs to target the region of separated flow. The overall methodology for both model ROM identification of actuator dynamics and optimal control sequence is illustrated in Figure 8.

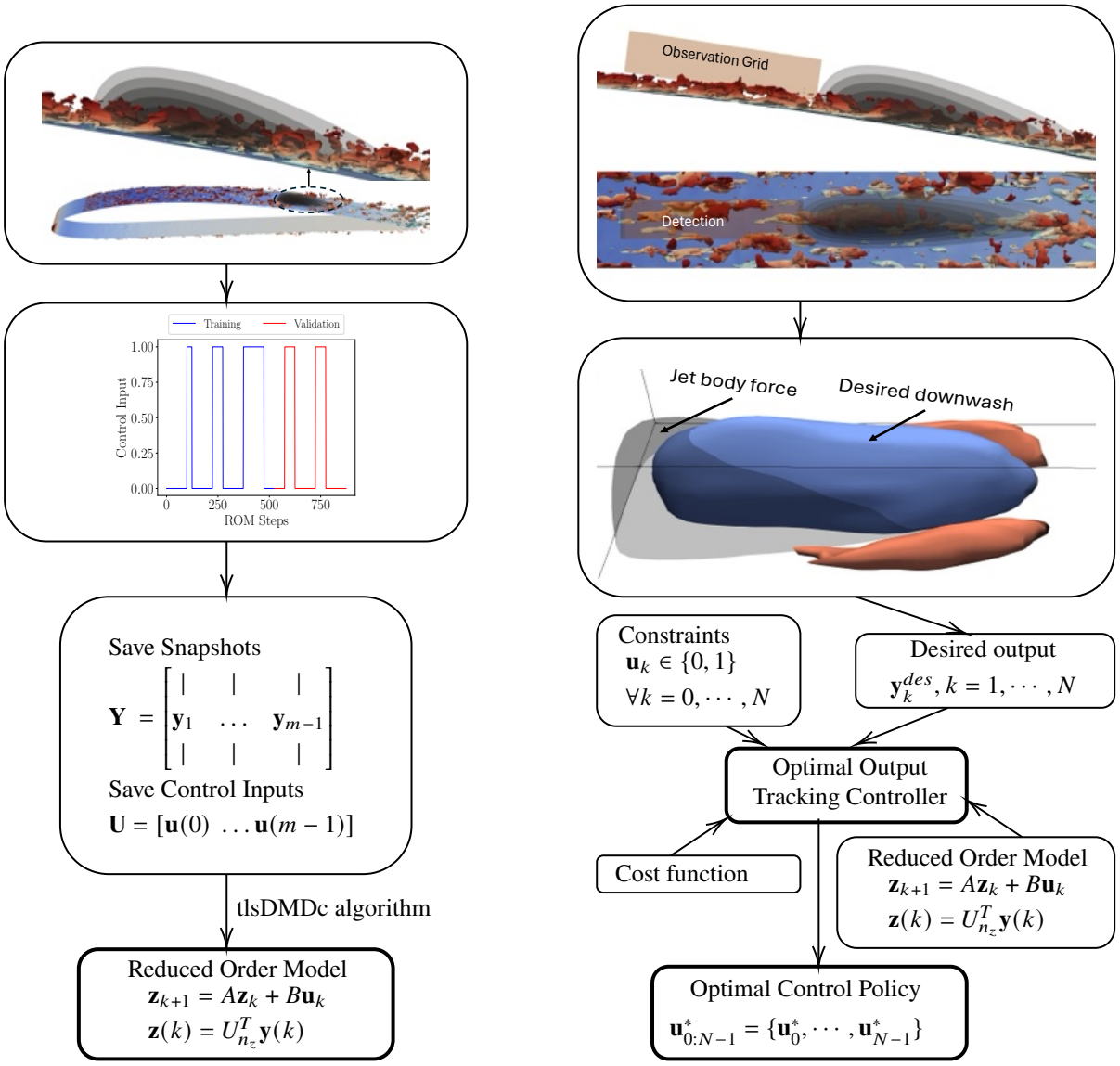

(a) Identification of ROM of the jet body-force using tlsDMDc **(b) Computing optimal output control sequence**

Fig. 8 Overview of the MPC methodology (a) deriving reduced order model (b) finding optimal control sequence for desired induced downwash from the jet actuator

C. Total Least-Squares Dynamic Mode Decomposition with Control

Following the objective of controlling LSMs in a turbulent flow via jet-induced downwash, it is essential to understand how the jet reacts in the presence of TBLs. The purpose of the tlsDMDc method is to derive a linear ROM of the system's dynamics when the full system dynamics are either unknown or computationally expensive to resolve in real time. This approach relies on a limited set of noisy experimental or numerical data, which is common in fluid dynamics applications.

Given a set of $m+1$ ensemble-averaged high-dimensional snapshots of the velocity field $\mathbf{y}(k)$, $k = 0, \ldots, m$,

generated from a sequence of inputs $\mathbf{u}(k)$, $k = 0, \ldots, m-1$, the data can be organized as:

$$\mathbf{Y} = \begin{bmatrix} \mathbf{y}(0) & \cdots & \mathbf{y}(m-1) \end{bmatrix} \in \mathbb{R}^{n_q \times m}, \tag{6a}$$

$$\mathbf{Y}' = \begin{bmatrix} \mathbf{y}(1) & \cdots & \mathbf{y}(m) \end{bmatrix} \in \mathbb{R}^{n_q \times m}, \tag{6b}$$

$$\mathbf{U} = \begin{bmatrix} \mathbf{u}(0) & \cdots & \mathbf{u}(m-1) \end{bmatrix} \in \mathbb{R}^{n_p \times m}. \tag{6c}$$

Since the states $\mathbf{y}(k)$ are high-dimensional, it it possible to identify a low-dimensional system using proper orthogonal decomposition (POD) using singular value decomposition (SVD),

$$\mathbf{Y} = U \Sigma V^T \tag{7}$$

The columns of the matrix $U \in \mathbb{R}^{n_q \times m}$ represent the POD modes arranged by the energy content. The high-dimensional state can than be mapped to an equivalent low-dimensional state using Eq. (8), where $U_{n_z} \in \mathbb{R}^{n_q \times n_z}$ is the POD mode matrix constructed from the first n_z most energetic modes. For this study, a total of $n_z = 10$ POD modes were used to balance between satisfactory model accuracy and prediction capability. In addition,

$$\mathbf{z}(k) = U_{n_z}^T \mathbf{y}(k) \tag{8}$$

where $\mathbf{z}(k)$ is the reduced-order state and $\mathbf{y}(k)$ is the original high-dimensional state (e.g., the flow field).

Assuming the high-dimensional system dynamics are linear, as done in DMDc [36], the POD mode amplitudes $\mathbf{z}(k)$ will also follow a linear state-space model, given the linearity of the POD projection. Following Ref. [37], to account for the noise in the data, it is assumed that the snapshots can be decomposed into a mean part and a noise part. The error in both components can be minimized by solving a relevant least-squares minimization problem. The final outcome of tlsDMDc is a reduced-order state-space model of the form:

$$\mathbf{z}(k+1) = A\mathbf{z}(k) + B\mathbf{u}(k) \tag{9}$$

where $A \in \mathbb{R}^{n_r \times n_r}$ and $B \in \mathbb{R}^{n_r \times n_p}$ are the state and input matrices, respectively. The detailed solution approach for this model is provided in Appendix A of Ref. [23].

D. Model Predictive Optimal Output Tracking Controller

Now that both the streamwise velocity fluctuations within the control grid (predicted via Taylor's hypothesis) and the jet actuator model dynamics (Eq. 9) are known, determining an optimal control input to maximize the downwash encountered by the LSMs can be formulated as an optimization problem. The problem, as restated from Ref. [23], is defined as follows:

$$\begin{aligned} \mathbf{u}^*_{t:t+Nmpc-1} = \underset{\mathbf{u}_{t:t+Nmpc-1}}{\arg\min} \quad & \sum_{k=t}^{t+N_{mpc}-1} \|p(k)\|_R^2 + \|\mathbf{y}(k+1) - \mathbf{y}_{des}(k+1)\|_Q^2 \\ \text{subject to} \quad & \mathbf{z}(k+1) = A\mathbf{z}(k) + Bp(k),\ k = t, \ldots, t+N_{mpc}-1 \\ & \mathbf{y}(k) = C\mathbf{z}(k),\ k = t, \ldots, t+N_{mpc} \\ & p(k) \in \{0,\ G\},\ k = t, \ldots, t+N_{mpc}-1 \\ & \mathbf{z}(t) = \tilde{\mathbf{z}}(t). \end{aligned} \tag{10}$$

The goal in the optimization problem given by Eq. (10) is to minimize the cost function by ensuring that the control input is minimized while reducing the error between the desired downwash and the predicted state. Here, Q and R are weighting matrices that penalize output deviations and control effort, respectively. $\tilde{\mathbf{z}}(k)$ denotes the previous estimate of the ROM state before new measurements are incorporated. $\mathbf{y}_{des}$ represents the desired downwash velocity, specifically the induced v' resulting from jet actuation. If $\mathbf{v}(k)$ denotes the vectorized predicted u' within the control grid, then, for the purpose of targeting high-momentum LSMs, $\mathbf{y}_{des}$ can be defined as:

$$\mathbf{y}_{des}(k) = -\lambda \mathbf{v}(k), \quad \forall k = 1, \cdots N_{mpc} \tag{11}$$

λ is a scaling factor that maps regions of high-momentum ($u' > 0$) to the desired downwash velocity. To produced downwash while targeting either fast or slow LSMs, λ is set to be a positive value to target fast LSMs and negative to

target slow LSMs. The optimization problem is solved over a control time horizon of $N_{mpc} = 50$ ROM time steps. Since new measurements are captured every $N_{meas} = 10$ ROM time steps, only the first 10 optimal inputs are applied before re-solving the problem. The detailed solution approach for this program is provided in Appendix B of Ref. [23].

V. Results

Before implementing the proposed control scheme outlined in Section IV and Subsections IV.B, IV.C, and IV.D, an LES simulation was performed to test the grid and determine the parameters associated with the tripping forces. Figure 9 illustrates the mean streamwise velocity field (Figure 9a) and an instantaneous streamwise velocity field (Figure 9b) over a NACA4412 airfoil at $Re_c = 200,000$ and $\alpha = 0°$. The mean lift coefficient $C_l = 0.37$ and drag coefficient $C_d = 0.17$, closely match the XFOIL prediction for a tripped NACA4412 airfoil at this Reynolds number $Re_c = 200,000$ and $\alpha = 0°$ [38].

LSMs of interest can be extracted using Reynolds decomposition: $u = \overline{U} + u'$, where $\overline{U}$ is the time-averaged component and u' is the fluctuating part. Figure 3b highlights LSMs with regions of momentum surplus for $u' > 0$. Figure 9b also highlights a very small incipient separation bubble near the trailing edge of the airfoil in the region of APG. The influence of APG increases with increasing α, promoting a larger region of separated flow.

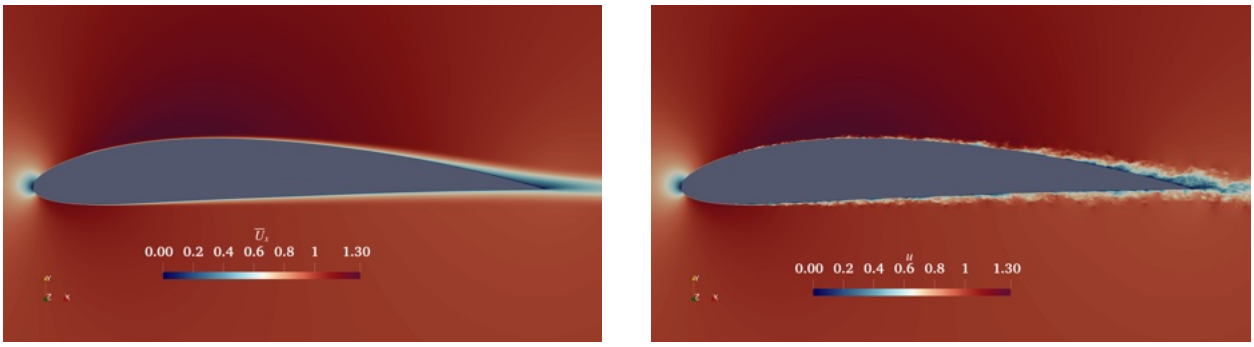

(a) Mean streamwise velocity field of tripped TBL **(b) Instantaneous streamwise velocity field of tripped TBL**

Fig. 9 Streamwise velocity fields over NACA4412 airfoil at $Re_c = 200,000$ and $\alpha = 0°$

A. Constant Jet Actuation

As described in Subsection III.A.2, a body force is modeled as a jet actuator to induce local flow acceleration in the streamwise velocity and downwash in the wall-normal velocity. Evaluating the influence of constant jet actuation on separated flow is essential, as these results will be compared with cases where fast and slow LSMs are targeted to assess performance improvements. To investigate separation under controlled conditions, the airfoil angle of attack was increased to $\alpha = 10°$ to achieve trailing-edge separation. Three different jet strengths were analyzed: $\mathbf{G} = 0$, $\mathbf{G} = 2.5$, and $\mathbf{G} = 5$, with $\mathbf{G} = 0$ representing the no-control case without jet actuation.

As shown in Figure 10, all three cases were run with steady and constant-power jet actuation for a period of $10c/V_\infty$ time units. During this period, running averages were computed to determine the mean effect on the separated volume near the trailing edge. The figure demonstrates that the total time-averaged volume occupied by the separated flow ($u < 0$) is significantly reduced as the jet strength increases.

Table 1 summarizes the mean lift and drag coefficients for each case. The lift and drag coefficients are computed using total surface integral of pressure and viscous forces and it does not account for reaction produced by the jet. In all three cases, the mean drag coefficient, C_d, remains nearly unchanged, indicating that the introduction of the external force field does not increase the total drag experienced by the airfoil. Conversely, the lift coefficient, C_l, shows improvement over the baseline case ($\mathbf{G} = 0$). Notably, for the strong jet case, C_l has increased by 8.97%. These results are promising; however, since constant jet actuation does not account for the presence of LSMs, targeting fast LSMs could potentially yield even greater benefits with reduced control efforts. This aspect is further analyzed and discussed in the following section.

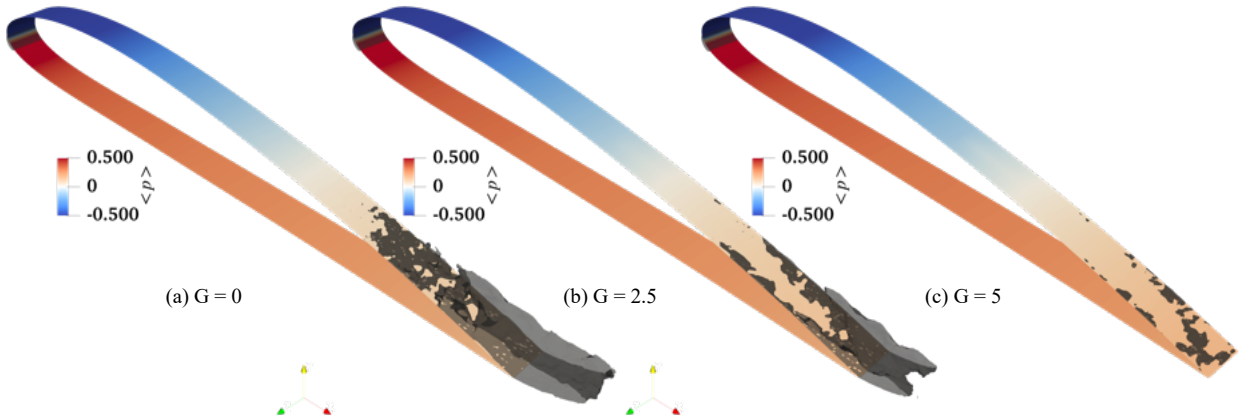

Fig. 10 Mean separation bubble (gray contour of $u = 0$) near the trailing edge for three different jet strengths (G). The airfoil is colored by the mean pressure distribution

Case	Jet Power (**G**)	C_l	C_d
No Jet	0	1.17	0.036
Moderate Jet	2.5	1.224 (+4.61%)	0.036
Strong Jet	5	1.275 (+8.97%)	0.035

Table 1 Mean lift and drag coefficients for different jet power

B. Targeting LSMs

To qualitatively assess the performance of the control scheme, five different test cases were run and compared. The cases are as follows: (1) Fast LSMs: $u' > 0$ was detected and targeted with $\lambda > 0$. (2) Slow LSMs: $u' < 0$ was detected and targeted with $\lambda > 0$. (3) Random Actuation: A random signal was generated with the same duty cycle and frequency as of for fast and slow LSMs case without any direct correlation to the presence of LSMs (4) Constant Jet Actuation: A constant jet actuation with half the jet power since the fast/slow LSM cases had about a 50% duty cycle, ensuring the same total power input over time. (5) Baseline (No Control): No jet actuation, with zero jet power. These cases provide a comparative framework to evaluate the effectiveness of the control strategies in influencing flow behavior.

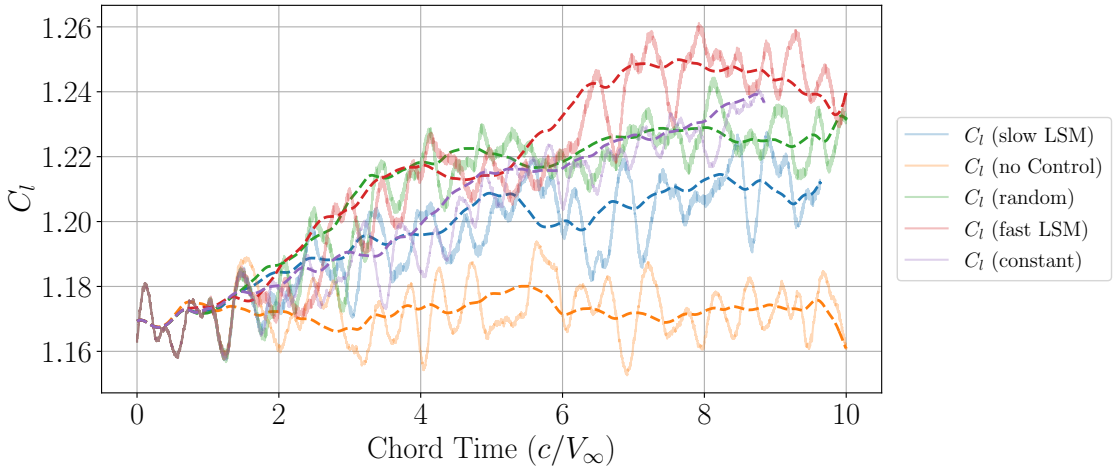

Fig. 11 Coefficient of lift C_l vs. chord-based time units for 5 different test cases: (1) Slow LSMs (blue) (2) No control (yellow) (3) Random (green) (4) Fast LSMs (red) (5) Constant (purple). Lighter shades show the instantaneous C_l value, while dashed lines are mean trend lines

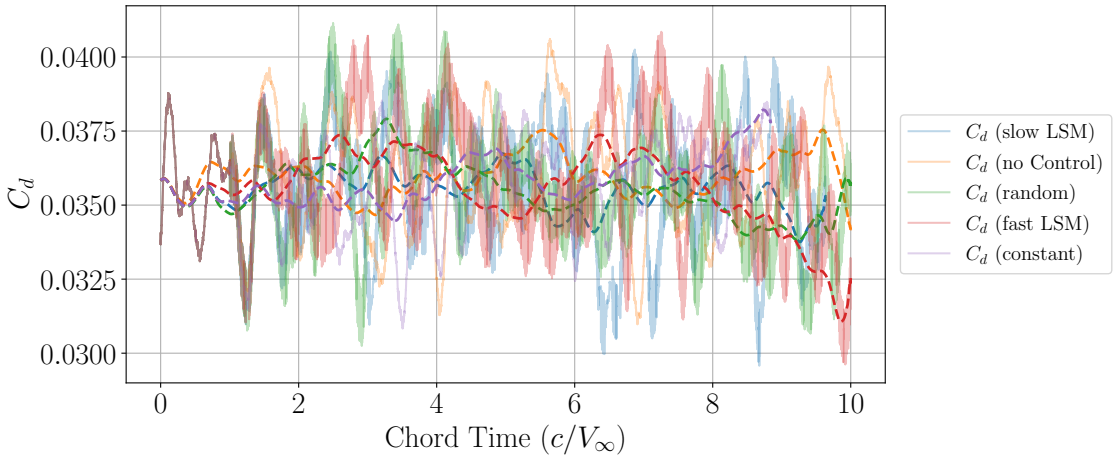

Fig. 12 Coefficient of drag C_d vs. chord-based time units for 5 different test cases: (1) Slow LSMs (blue) (2) No control (yellow) (3) Random (green) (4) Fast LSMs (red) (5) Constant (purple). Lighter shades show the instantaneous C_l value, while dashed lines are mean trend lines

Figures 11 and 12 illustrate the variations in C_l and C_d across the five different cases over a total of $10c/V_\infty$ time units. Due to the high computational cost of these simulations, obtaining statistics over extended periods becomes impractical. All simulations started with the same initial conditions and identical random number generation for the tripping forces, ensuring that each case experienced "the same" turbulence before encountering the jet. This consistency is evident in the figures, as the C_l and C_d values show no deviations across any cases during the first chord-based time unit before the MPC module was initiated. The MPC module in the LES simulation was activated after $1c/V_\infty$ time unit, allowing sufficient time for the time-averaged velocity to reach a statistically steady state.

As shown in Figure 11, a transient behavior is evident before the C_l values appear to stabilize to a steady state. This transient occurs between $c/V_\infty = 2$ and 6 across all cases, except for the baseline case without any control or jet actuation. Like the constant jet case (Table 1), the C_d values show minimal variation across all five cases under consideration. The observed fluctuations in C_d are in the same order as those in the baseline case without control.

Case	Jet Power (**G**)	C_l	C_d	C_l/C_d
Baseline	0	1.17	0.036	32.67
Constant Jet	2.5	1.224 (+4.61%)	0.036	33.99
Random Jet	5	1.224 (+4.61%)	0.035	35.10
Slow LSMs	5	1.206 (+3.08%)	0.036	34.40
Fast LSMs	5	1.243 (+6.24%)	0.036	35.1

Table 2 Mean lift and drag coefficients for different cases

Table 2 summarizes C_l and C_d, as well as C_l/C_d, for five different control cases, averaged over $c/V_\infty = 6$ and 10, after initial transient has passed. The baseline case, with no jet actuation ($G = 0$), has a mean C_l of 1.17 and C_d of 0.036. Different control strategies, including constant jet actuation, random actuation, and targeting fast and slow LSMs, demonstrate varying levels of improvement in C_l without significantly impacting C_d. Notably, the fast LSMs case achieves the highest lift enhancement, with C_l increased by 6.24% while maintaining the same C_d as the baseline. This results in the highest C_l/C_d ratio of 35.1 among all cases, indicating a significant improvement in aerodynamic efficiency. These results highlight the potential of LSM-targeted strategies in achieving superior lift performance compared to other jet actuation strategies.

VI. Conclusion and Discussion

In this study, an MPC model was applied to turbulent flow over a NACA4412 airfoil at a chord-based moderate Reynolds number of $Re_c = 200,000$ and an angle of attack $\alpha = 10°$, as part of an active flow control methodology

targeting LSMs. The proposed method utilizes an observation grid to detect and identify fast- and slow-moving LSMs. Using Taylor's hypothesis, the future trajectories of these LSMs are predicted and incorporated into the ROM of the jet within the optimal control framework to generate downwash for the targeted structures. A formal analysis was conducted to compare various actuation schemes, including those targeting fast and slow LSMs, as well as random and constant actuation, against the baseline case without actuation.

As shown in Section V, the greatest improvements were observed when fast LSMs were targeted, as hypothesized. It is important to note that a steady jet with increasing strength could potentially outperform the proposed approach, but this comes at the expense of higher control effort, i.e., total power consumption (force times velocity). This power requirement can be significantly reduced by directing fast LSMs toward the adverse pressure gradient region. Additionally, while the current study considers a moderate Reynolds number, the effectiveness of the methodology at higher Reynolds numbers remains to be evaluated. Nevertheless, the concept is expected to hold, as higher Reynolds numbers generally produce more energetic and larger turbulent structures [39].

The present study builds upon the findings of Tsolovikos et al. [23], where an MPC model was employed to identify and control LSMs for active flow control, effectively reducing the size and volume of the separated region in the TBL over a flat plate. This work extends the approach to a more practical and realistic scenario by applying the control framework to flow over an airfoil. However, as this research focuses on demonstrating proof of concept, several design choices were made that are not fully optimized. For instance, the spanwise domain length was kept relatively small, accommodating only a single actuator. In practice, it is feasible to envision a series of jet actuators distributed along the span, working collectively to enhance aerodynamic performance and efficiency. Various other parameter spaces were left unexplored due to computational limitations, including jet model parameters such as the placement of the jet relative to the separated flow, pitch angle, and other configuration details.

VII. Future Work

This study demonstrates a proof of concept at a moderate Reynolds number; however, future work will include simulations at higher Reynolds numbers, such as $Re_c = 400,000$, at appropriate angles of attack to induce sufficiently large separation near the trailing edge. Additionally, advanced variants of the DMD model, such as online DMDc (oDMDc) [40], will be tested to actively learn the flow dynamics and develop a reduced-order model of the flow interactions. This real-time system identification capability will enable the control strategy to adapt to changing flow conditions, enhancing its effectiveness in managing flow separation at higher angles of attack and Reynolds numbers.

To further refine the control mechanism, more robust learning algorithms, combining tlsDMDc and oDMDc, will be implemented. This integrated approach will account for the dynamics of the separated flow while incorporating the control input from the jet body force and its effects on the DMD modes of the separation bubble, providing a more comprehensive and adaptive framework for flow control.

VIII. Acknowledgement

The authors would like to acknowledge support by NSF Award Nos. 2129494 and 2052811, as well as the Texas Advanced Computing Center (TACC) at The University of Texas at Austin for providing HPC resources that have contributed to support this work.

References

[1] Robinson, S. K., "Coherent motions in the turbulent boundary layer," *Annu. Rev. Fluid Mech*, Vol. 23, No. 1, 1991. https://doi.org/10.1146/annurev.fl.23.010191.003125.

[2] Liu, Z., Adrian, R. J., and Hanratty, T. J., "Large-scale modes of turbulent channel flow: transport and structure," *Journal of Fluid Mechanics*, Vol. 448, 2001, pp. 53–80.

[3] Kim, K. C., and Adrian, R. J., "Very large-scale motion in the outer layer," *Physics of Fluids*, Vol. 11, No. 2, 1999, pp. 417–422. https://doi.org/10.1063/1.869889.

[4] Dennis, D. J. C., and Nickels, T. B., "Experimental measurement of large-scale three-dimensional structures in a turbulent boundary layer. Part 2. Long Structures," *Journal of Fluid Mechanics*, Vol. 673, 2011, pp. 218–244. https://doi.org/10.1017/S0022112010006324.

[5] Jiménez, J., "Coherent structures in wall-bounded turbulence," *Journal of Fluid Mechanics*, Vol. 842, 2018, p. P1. https://doi.org/10.1017/jfm.2018.144.

[6] Hutchins, N., and Marusic, I., "Evidence of very long meandering features in the logarithmic region of turbulent boundary layers," *Journal of Fluid Mechanics*, Vol. 579, 2007, pp. 1–28.

[7] Krogstad, P.-Å., and Skåre, P. E., "Influence of a strong adverse pressure gradient on the turbulent structure in a boundary layer," *Physics of Fluids*, Vol. 7, No. 8, 1995, pp. 2014–2024.

[8] Harun, Z., Monty, J. P., Mathis, R., and Marusic, I., "Pressure gradient effects on the large-scale structure of turbulent boundary layers," *Journal of Fluid Mechanics*, Vol. 715, 2013, pp. 477–498.

[9] Rahgozar, S., and Maciel, Y., "Low-and high-speed structures in the outer region of an adverse-pressure-gradient turbulent boundary layer," *Experimental thermal and fluid science*, Vol. 35, No. 8, 2011, pp. 1575–1587.

[10] Lee, J. H., "Large-scale motions in turbulent boundary layers subjected to adverse pressure gradients," *Journal of Fluid Mechanics*, Vol. 810, 2017, pp. 323–361.

[11] Lee, J.-H., and Sung, H. J., "Structures in turbulent boundary layers subjected to adverse pressure gradients," *Journal of fluid mechanics*, Vol. 639, 2009, pp. 101–131.

[12] Atzori, M., Vinuesa, R., Fahland, G., Stroh, A., Gatti, D., Frohnapfel, B., and Schlatter, P., "Aerodynamic effects of uniform blowing and suction on a NACA4412 airfoil," *Flow, Turbulence and Combustion*, Vol. 105, No. 3, 2020, pp. 735–759.

[13] Atzori, M., Vinuesa, R., Stroh, A., Gatti, D., Frohnapfel, B., and Schlatter, P., "Uniform blowing and suction applied to nonuniform adverse-pressure-gradient wing boundary layers," *Physical Review Fluids*, Vol. 6, No. 11, 2021, p. 113904.

[14] Corke, T. C., Enloe, C. L., and Wilkinson, S. P., "Dielectric barrier discharge plasma actuators for flow control," *Annual review of fluid mechanics*, Vol. 42, 2010, pp. 505–529.

[15] Abbassi, M., Baars, W., Hutchins, N., and Marusic, I., "Skin-friction drag reduction in a high-Reynolds-number turbulent boundary layer via real-time control of large-scale structures," *International Journal of Heat and Fluid Flow*, Vol. 67, 2017, pp. 30–41.

[16] Marusic, I., Talluru, K., and Hutchins, N., "Controlling the large-scale motions in a turbulent boundary layer," *Fluid-Structure-Sound Interactions and Control: Proceedings of the 2nd Symposium on Fluid-Structure-Sound Interactions and Control*, Springer, 2014, pp. 17–26.

[17] Karniadakis, G., and Choi, K.-S., "Mechanisms on transverse motions in turbulent wall flows," *Annual review of fluid mechanics*, Vol. 35, No. 1, 2003, pp. 45–62.

[18] Rathnasingham, R., and Breuer, K. S., "Active control of turbulent boundary layers," *Journal of Fluid Mechanics*, Vol. 495, 2003, pp. 209–233.

[19] Moin, P., and Bewley, T., "Feedback control of turbulence," *Applied Mechanics Review,*, 1994.

[20] Tsolovikos, A., Suryanarayanan, S., Bakolas, E., and Goldstein, D., "Model predictive control of material volumes with application to vortical structures," *AIAA Journal*, Vol. 59, No. 10, 2021, pp. 4057–4070.

[21] Jariwala, A., Tsolovikos, A., Suryanarayanan, S., Goldstein, D. B., and Bakolas, E., "On the effect of manipulating Large Scale Motions in a Boundary Layer," *AIAA AVIATION 2022 Forum*, 2022, p. 3771.

[22] Wylie, J., and Amitay, M., "Control of Artificially-Generated Hairpin Vortices in a Laminar Boundary Layer," *AIAA SCITECH 2024 Forum*, 2024, p. 0928.

[23] Tsolovikos, A., Jariwala, A., Suryanarayanan, S., Bakolas, E., and Goldstein, D., "Separation delay in turbulent boundary layers via model predictive control of large-scale motions," *Physics of Fluids*, Vol. 35, No. 11, 2023.

[24] Schlatter, P., and Örlü, R., "Turbulent boundary layers at moderate Reynolds numbers: inflow length and tripping effects," *Journal of Fluid Mechanics*, Vol. 710, 2012, pp. 5–34.

[25] Brauner, T., Laizet, S., Benard, N., and Moreau, E., "Modelling of dielectric barrier discharge plasma actuators for direct numerical simulations," *8th AIAA Flow Control Conference*, 2016, p. 3774.

[26] Gildersleeve, S., and Amitay, M., "Three-dimensional wake characteristics associated with the jet assisted surface mounted actuator," *2018 Flow Control Conference*, 2018, p. 3060.

[27] Paul F. Fischer, J. W. L., and Kerkemeier, S. G., "nek5000 Web page," , 2008. Http://nek5000.mcs.anl.gov.

[28] Schlatter, P., Stolz, S., and Kleiser, L., "LES of transitional flows using the approximate deconvolution model," *International journal of heat and fluid flow*, Vol. 25, No. 3, 2004, pp. 549–558.

[29] Massaro, D., Peplinski, A., Stanly, R., Mirzareza, S., Lupi, V., Mukha, T., and Schlatter, P., "A comprehensive framework to enhance numerical simulations in the spectral-element code Nek5000," *Computer Physics Communications*, Vol. 302, 2024, p. 109249.

[30] Vinuesa, R., Negi, P. S., Atzori, M., Hanifi, A., Henningson, D. S., and Schlatter, P., "Turbulent boundary layers around wing sections up to Rec= 1,000,000," *International Journal of Heat and Fluid Flow*, Vol. 72, 2018, pp. 86–99.

[31] Hosseini, S. M., Vinuesa, R., Schlatter, P., Hanifi, A., and Henningson, D. S., "Direct numerical simulation of the flow around a wing section at moderate Reynolds number," *International Journal of Heat and Fluid Flow*, Vol. 61, 2016, pp. 117–128.

[32] Atzori, M., Vinuesa, R., Lozano-Durán, A., and Schlatter, P., "Coherent structures in turbulent boundary layers over an airfoil," *Journal of Physics: Conference Series*, Vol. 1522, IOP Publishing, 2020, p. 012020.

[33] Tsolovikos, A., Jariwala, A., Suryanarayanan, S., Bakolas, E., and Goldstein, D., "Separation Delay in Turbulent Boundary Layers via Model Predictive Control of Large-Scale Motions," *Bulletin of the American Physical Society*, 2022.

[34] Taylor, G. I., "The spectrum of turbulence," *Proceedings of the Royal Society of London. Series A-Mathematical and Physical Sciences*, Vol. 164, No. 919, 1938, pp. 476–490.

[35] Dennis, D. J., and Nickels, T. B., "On the limitations of Taylor's hypothesis in constructing long structures in a turbulent boundary layer," *Journal of Fluid Mechanics*, Vol. 614, 2008, pp. 197–206.

[36] Proctor, J. L., Brunton, S. L., and Kutz, J. N., "Dynamic mode decomposition with control," *SIAM Journal on Applied Dynamical Systems*, Vol. 15, No. 1, 2016, pp. 142–161.

[37] Dawson, S., Hemati, M. S., Williams, M. O., and Rowley, C. W., "Characterizing and correcting for the effect of sensor noise in the dynamic mode decomposition," *Exp. in Fluids*, Vol. 57, No. 3, 2016, pp. 1–19.

[38] Drela, M., "XFOIL: An analysis and design system for low Reynolds number airfoils," *Low Reynolds Number Aerodynamics: Proceedings of the Conference Notre Dame, Indiana, USA, 5–7 June 1989*, Springer, 1989, pp. 1–12.

[39] Lee, J. H., and Sung, H. J., "Very-large-scale motions in a turbulent boundary layer," *Journal of Fluid Mechanics*, Vol. 673, 2011, pp. 80–120.

[40] Deem, E. A., Cattafesta, L. N., Hemati, M. S., Zhang, H., Rowley, C., and Mittal, R., "Adaptive separation control of a laminar boundary layer using online dynamic mode decomposition," *Journal of Fluid Mechanics*, Vol. 903, 2020, p. A21.